


 Cite this: *RSC Adv.*, 2021, **11**, 19136

## Preparation and electrochemical properties of a novel porous $\text{Ti/Sn-Sb-RuO}_x/\beta\text{-PbO}_2/\text{MnO}_2$ anode for zinc electrowinning

 Buming Chen,<sup>ac</sup> Jianhua Liu,  <sup>\*ab</sup> Shichuan Wang,<sup>\*ab</sup> Hui Huang,<sup>ac</sup> Yapeng He<sup>ac</sup> and Zhongcheng Guo<sup>ac</sup>

$\text{MnO}_2$  coatings prepared in a sulfate system ( $\text{S-MnO}_2$ ) and  $\text{MnO}_2$  prepared in a nitrate system ( $\text{N-MnO}_2$ ) were successfully deposited on porous  $\text{Ti/Sn-Sb-RuO}_x/\beta\text{-PbO}_2$  substrates by electrodeposition, and their electrochemical properties were studied in detail. The bath composition plays a very important role in the  $\text{MnO}_2$  coating prepared by electrodeposition at a low current density. The results of scanning electron microscopy show that a  $\text{Ti/Sn-Sb-RuO}_x/\beta\text{-PbO}_2/\text{MnO}_2$  electrode has a rough morphology and the unit cell is very good. At the same time, the surface cracks in the  $\text{S-MnO}_2$  coating are larger than those in the  $\text{N-MnO}_2$  coating. In addition, the  $\text{N-MnO}_2$  coating is composed of a fluffy sheet-like substance. The surface morphology of the  $\text{N-MnO}_2$  coating is denser than that of the  $\text{S-MnO}_2$  coating. The  $\text{S-MnO}_2$  coating consists of irregularly stacked granular particles. Further, the main crystal phase of  $\text{MnO}_2$  is  $\gamma$  type, and the main valence state of  $\text{MnO}_2$  is +4. The results show that the oxygen evolution potential of the  $\text{N-MnO}_2$  electrode is 63 mV lower than that of the  $\text{S-MnO}_2$  electrode, indicating that the  $\text{N-MnO}_2$  electrode has better oxygen evolution activity and electrochemical stability, which can also be confirmed by EIS test results. Under the accelerated life test conditions, the  $\text{N-MnO}_2$  electrode has a better service life of 77 h at a current density of  $1 \text{ A cm}^{-2}$  in  $150 \text{ g L}^{-1} \text{ H}_2\text{SO}_4$  and  $2 \text{ g L}^{-1} \text{ Cl}^-$  solution.

 Received 11th April 2021  
 Accepted 19th May 2021

 DOI: 10.1039/d1ra02815d  
[rsc.li/rsc-advances](http://rsc.li/rsc-advances)

### 1. Introduction

The oxygen evolution reaction (OER) is the primary anode reaction in the zinc electrowinning (EW) process, and the overpotential of the anode material directly determines the cell voltage and energy consumption of the process. In recent years, lead alloy and titanium-based electrode materials have been mostly used in the hydrometallurgical industry and in the EW field. Conventional lead-based anodes used in zinc EW are associated with high corrosion rates and oxygen evolution overpotential. However, both electrodes (lead and titanium) suffer from issues such as large internal resistance. In sulphate electrolyte, the active oxygen generated by the electrolysis reaction is immersed in the surface of the titanium substrate, generating passivation on the surface of the titanium substrate and forming an oxide film (*i.e.*  $\text{TiO}_2$ ). Manganese ions, which typically exist in zinc EW electrolyte, can influence anode performance, depending on their concentration and the anode material. Therefore, the authors developed a new composite

anode by using  $\text{MnO}_2$  particles in a composite matrix to improve anode performance under zinc EW operating conditions.<sup>1,2</sup> A recent report showed that  $\text{MnO}_2$  is an oxygen evolution anode that is only less active than  $\text{RuO}_2$  and  $\text{IrO}_2$ .<sup>3</sup> However, its stability is poor, and this condition is related to the nature of manganese. As a transition metal, manganese has a special d-electron shell structure.<sup>4</sup> In accordance with Jahn-Teller theory, ions with an asymmetric d-electron shell structure deviate from normal octahedrons or regular tetrahedrons.<sup>5</sup> Manganese oxide is a typical representative of Betolai (*i.e.* nonspecific) compounds, and its structure is extremely varied. The representative oxide of  $\text{MnO}_2$  is actually an oxide between  $\text{MnO}_{1.7}$  and  $\text{MnO}_2$ . Given the special d-electron shell structure of manganese, its oxides are mostly in nonequilibrium phases, with numerous lattice defects and distortion.<sup>6</sup> The atom at the defect, whether it is a surface or point defect, is in a high energy state, generating chemical activities in the crystal. Therefore,  $\text{MnO}_2$  is currently recognised as one of the most electrochemically active electrode materials.<sup>7</sup> However, it exhibits the disadvantages of low processing strength and short service life.<sup>8</sup>

As a new type of anode, a titanium-based  $\text{MnO}_2$  anode does not easily dissolve during the electrolysis process; it also does not pollute EW products, can produce high-purity metals and has high mechanical strength; thus, it prevents cathode-anode short circuit, corrosion resistance and low energy consumption.<sup>9</sup>

<sup>a</sup>Faculty of Metallurgical and Energy Engineering, Kunming University of Science and Technology, Kunming 650093, China. E-mail: liujianhua501050@163.com; kmustshichuanwang@163.com

<sup>b</sup>State Key Laboratory of Complex Nonferrous Metal Resources Clean Utilization, Kunming University of Science and Technology, Kunming 650093, China

<sup>c</sup>Kunming Hengda Technology Co. LTD., Kunming 650106, China



However, its conductivity and stability are not ideal, and this problem is solved by adding an intermediate layer.

Lead dioxide is widely used because of its good electrical conductivity, good mechanical properties, relatively low preparation cost, good chemical stability in acidic solutions, low oxygen evolution overpotential and relatively large specific surface area.<sup>10–12</sup> On this basis, porous lead dioxide was prepared because of its high electrocatalytic activity.<sup>13</sup> Simultaneously, given the unique surface morphology of porous lead dioxide, MnO<sub>2</sub> deposited on its surface will form a partially mosaic structure, improving the binding force between the two substances and the stability of the electrode.

MnO<sub>2</sub> electrodeposited under similar conditions from acidic solutions of manganese chloride, manganese nitrate or manganese perchlorate exhibits a clear fibrous structure. The axes of single fibres are parallel with the direction of growth. Fibrous MnO<sub>2</sub> exhibits an excellent orientation, a high degree of crystallisation and needle-shaped crystallites. Direct current resistance in the direction parallel to the direction of growth is considerably lower than the resistance in the direction normal to the direction of growth.<sup>14</sup>

We proposed a new preparation method for MnO<sub>2</sub> on a porous Ti/Sn–Sb–RuO<sub>x</sub>/β-PbO<sub>2</sub> substrate by using low current density. Surface morphology and phase were investigated by comparing MnO<sub>2</sub> electrodes prepared in two different plating baths. The composition and electrochemical properties of the electrode were investigated by using scanning electron microscopy (SEM), X-ray diffraction (XRD), X-ray photoelectron spectroscopy (XPS) and an electrochemical workstation. In addition, the stability of the electrode was studied *via* accelerated life testing.

## 2. Experiments

### 2.1. Preparation of electrodes

**2.1.1. Ti substrates pretreatment.** The first process, which included four steps, was the pretreatment of the titanium substrate.<sup>15</sup> Firstly, titanium plates (TA1) with dimensions of 20 mm × 20 mm × 1 mm were immersed in 10 wt% NaOH solution at 70 °C for 30 min and then washed with deionised (DI) water to remove grease or oil. Subsequently, the cleaned titanium plates were etched in mixed acid ( $V_{HF}/V_{HNO_3}/V_{H_2O} = 1 : 4 : 5$ ) for 3 min to remove the oxide layer and washed with DI water. Thereafter, the further cleaned titanium plates were etched in 20 wt% HCl solution at 90 °C for 120 min to form a rough surface. Finally, the pretreated titanium substrate was stored in a solution of ethanol and 2% oxalic acid at room temperature before use.

**2.1.2. Preparation of Sn–Sb–RuO<sub>x</sub> underlayer.** The precursor solution for Sn–Sb–RuO<sub>x</sub> preparation was a mixture of 3.0 M SnCl<sub>4</sub>·5H<sub>2</sub>O, 0.50 M SbCl<sub>3</sub>, 0.60 M HCl and 0.375 M RuCl<sub>3</sub>·3H<sub>2</sub>O in *n*-butanol solution. Then, the pretreated titanium substrates were painted with the precursor solution by using brushes. After being dried at 100 °C for 2 min, the substrates were heated at an annealing temperature of 500 °C for 10 min. After naturally cooling to room temperature, the sheets were brushed again. The entire procedure was repeated

eight times, and the samples were heated at the same annealing temperature for 1 h with a total oxide loading of approximately 8–10 g m<sup>-2</sup>.

**2.1.3. Preparation of porous β-PbO<sub>2</sub> interlayer.** In the process of PbO<sub>2</sub> interlayer formation, an electrodeposition method was used to form β-PbO<sub>2</sub> coating on the surface of the underlayer. The aqueous solution components were 0.8 M Pb(NO<sub>3</sub>)<sub>2</sub>, 0.1 M HNO<sub>3</sub> and 0.015 M Fe(NO<sub>3</sub>)<sub>3</sub>. The Ti/Sn–Sb–RuO<sub>x</sub> coating was used as the anode, and a titanium mesh of the same size was used as the cathode. The current density was controlled at 20 mA cm<sup>-2</sup>. The gap between the anode and the cathode was 20 mm. The deposition processes were performed at 60 °C for 2 h with mild stirring using a magnetic stirrer.

**2.1.4. Preparation of γ-MnO<sub>2</sub> toplayer.** In the process of active MnO<sub>2</sub> layer formation, an electrodeposition method was used to form γ-MnO<sub>2</sub> coating on the surface of the interlayer. The electrolyte composition was 0.89 M MnSO<sub>4</sub>·H<sub>2</sub>O + 0.1 M H<sub>2</sub>SO<sub>4</sub> or 0.42 M Mn(NO<sub>3</sub>)<sub>2</sub> + 0.16 HNO<sub>3</sub>. MnO<sub>2</sub> coatings were obtained *via* electrodeposition from the sulphate and nitrate baths and were respectively called S-MnO<sub>2</sub> and N-MnO<sub>2</sub> coatings. The Ti/Sn–Sb–RuO<sub>x</sub>/β-PbO<sub>2</sub> coating was used as the anode, and a titanium mesh of the same size was used as the cathode. The current density was controlled at 4 mA cm<sup>-2</sup>. The gap between the anode and the cathode was 20 mm. The deposition processes were performed at 60 °C for 2 h with mild stirring using a magnetic stirrer.

### 2.2. Characterization of electrodes

An electrochemical workstation (CS350, Corrtest, China) with three electrode systems was used to perform anodic polarisation, cyclic voltammetry (CV) and electrochemical impedance spectroscopy (EIS) in a synthetic electrolyte solution composed of 50 g L<sup>-1</sup> Zn<sup>2+</sup> and 150 g L<sup>-1</sup> H<sub>2</sub>SO<sub>4</sub> at 40 °C. The working electrode (WE) was the experimental samples with a working area of 1.0 cm<sup>2</sup>. The remaining areas were sealed with epoxy resin. The reference electrode (RE) was a saturated calomel electrode (SCE). The counter electrode (CE) consisted of a 6 cm<sup>2</sup> platinum plate. The scanning rate for the anodic polarisation curve was 10 mV s<sup>-1</sup>. The frequency interval of the EIS measurements ranged from 10<sup>5</sup> Hz to 10<sup>-1</sup> Hz, and the alternating current (AC) amplitude was 5 mV root mean squared. The applied anodic potential was 1.5 V (SCE). The impedance data were converted into Nyquist data format and then fitted into appropriate equivalent electrical.

The surface morphology of the anodic oxide layer was characterised *via* SEM by using a Philips XL30 environmental scanning electron microscope (Holland). XPS spectra were collected from samples by using a K-Alpha<sup>TM</sup> spectrometer (Thermo Fisher Scientific Inc., USA) to analyse the chemical composition. The analysed values of the binding energy (BE) were relative to the C 1s photoelectron line (BE = 284.8 eV). The phase composition of the films was studied *via* XRD by using a D8 ADVANCE diffractometer (Bruker, Germany) with Cu K-alpha radiation.

The service life of the two anode coatings was evaluated in a solution containing 2 g L<sup>-1</sup> Cl<sup>-</sup> and 150 g L<sup>-1</sup> sulphuric acid at



25 °C with a titanium mesh as the cathode. The distance between electrodes was 20 mm, and the current density was 1 A cm<sup>-2</sup>.

### 3. Results and discussion

#### 3.1. SEM analysis

Fig. 1 shows the SEM images of MnO<sub>2</sub> prepared *via* electrodeposition in different plating baths. The surface of Fig. 1a is densely packed with a large number of particles, exhibiting a dense and uniform structure. A large number of fine cracks are found on the surface of Fig. 1b, and surface granular morphology is evident. Simultaneously, the surface of MnO<sub>2</sub> prepared under both conditions has a pore-like morphology because the anode continues to evolve oxygen during the preparation of the electrode, and Mn<sup>2+</sup> is deposited onto the surface of the electrode along the adhered oxygen bubbles. In addition, Mn<sup>2+</sup> is deposited inside the pores because the electrode is porous. The surface morphology of the electrodes is covered to form a MnO<sub>2</sub> coating. As shown in Fig. 1c and d, these small particles are stacked on one another to form a relatively dense structure. The surface grain bonding of Fig. 1c

is tighter than that of Fig. 1d. Fig. 1e and f illustrate the structure of the reaction electrode at high magnification. The morphology of N-MnO<sub>2</sub> under microscopic appearance is ribbonlike, layered and densely bonded. The grain size is 50–150 nm. S-MnO<sub>2</sub> is microscopically shaped. The grains have a sharp grainy shape, which is intertwined and has many intergranular voids. Grain size is between 50 nm and 100 nm, and crystal grains are randomly stacked. The gap between crystal grains is larger, and thus, more conducive to the penetration of the electrolyte. The surface morphology of the two electrodes observed under high magnification can indicate that the electrolyte is more likely to penetrate into the S-MnO<sub>2</sub> coating and come in contact with the substrate during the use of the electrode.

With regard to the presence of pores and cracks on the surface of the Ti/Sn–Sb–RuO<sub>x</sub>/PbO<sub>2</sub>/MnO<sub>2</sub> coating, Fig. 2 shows a cross-sectional microscopy to evaluate the interface bonding state. Fig. 2a and c are SEM images of the N-MnO<sub>2</sub> coating. Fig. 2b is an SEM image of the S-MnO<sub>2</sub> coating. Fig. 2a and b show that PbO<sub>2</sub> and MnO<sub>2</sub> are tightly bonded, and no significant cracks are found in the MnO<sub>2</sub> layer. The average

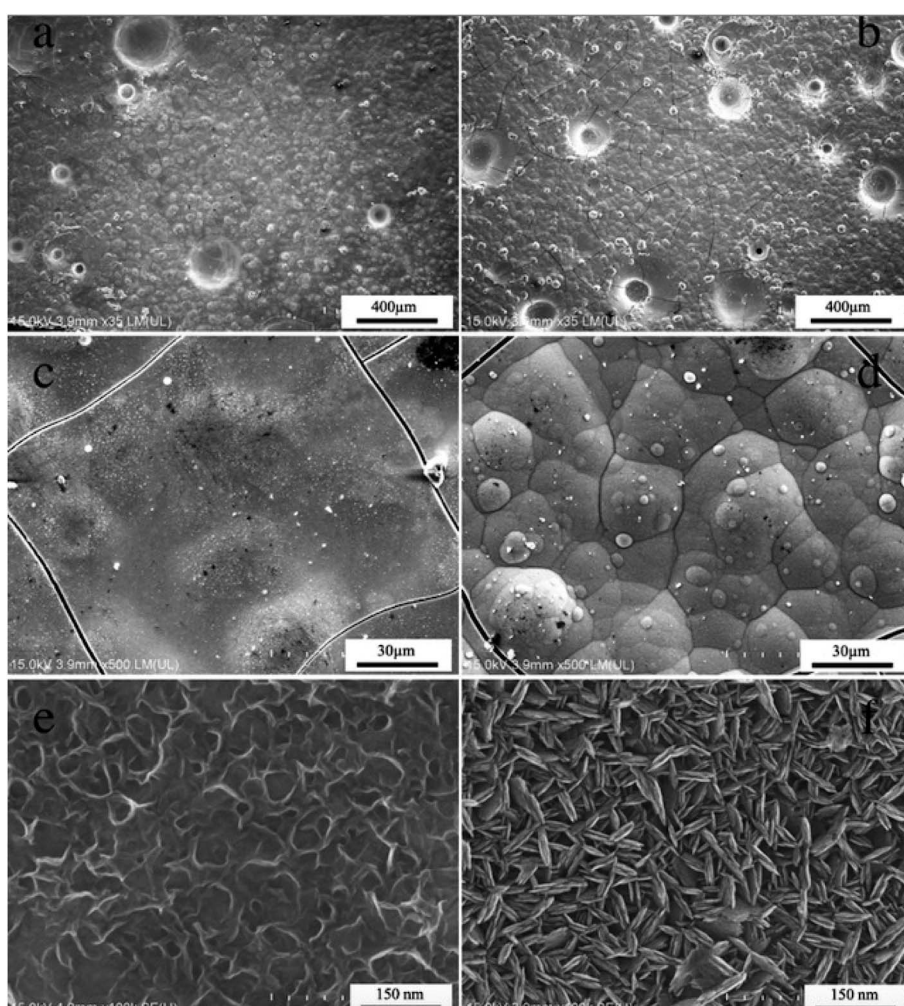


Fig. 1 SEM images of the Ti/Sn–Sb–RuO<sub>x</sub>/β-PbO<sub>2</sub>/MnO<sub>2</sub> coatings electrodeposited at different plating solution, (a, c, e) manganese nitrate solution, (b, d, f) manganese sulfate solution.



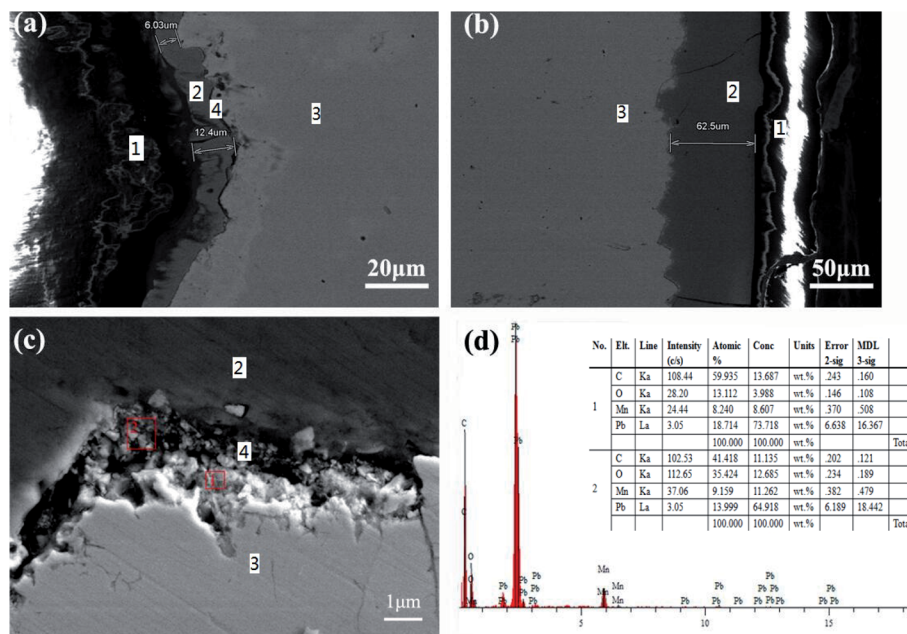


Fig. 2 a cross-sectional microscopy of the Ti/Sn-Sb-RuO<sub>x</sub>/β-PbO<sub>2</sub>/MnO<sub>2</sub> coatings, 20 μm scale (a), 1 μm scale (c) and EDS patterns (d) of the N-MnO<sub>2</sub> coating, 50 μm scale (b) of the S-MnO<sub>2</sub> coating; marks (1)–(4) refer to the epoxy resin, MnO<sub>2</sub> coating, PbO<sub>2</sub> coating, and Pb-MnO<sub>x</sub> transition layer, respectively.

thickness of the N-MnO<sub>2</sub> plating layer in Fig. 2a is 9.21 μm, and the average thickness of the S-MnO<sub>2</sub> plating layer in Fig. 2b is 62.5 μm. The high-magnification SEM image in Fig. 2c shows a significant Pb-MnO<sub>x</sub> transition layer during the electrodeposition of MnO<sub>2</sub> in the nitric acid system. This phenomenon may be due to the reaction of PbO<sub>2</sub> with Mn<sup>2+</sup> in the nitric acid system to form a mixture.

### 3.2. XRD analysis

Fig. 3 shows the XRD patterns of the S-MnO<sub>2</sub> and N-MnO<sub>2</sub> coatings. The peak positions of the two materials are basically identical, and only a difference in peak intensity exists. The major peaks are all diffraction peaks of MnO<sub>2</sub>; however, other

weaker peaks can be observed, including oxides of lead and manganese, mixed oxides of lead and manganese and trace PbSO<sub>4</sub> (for the S-MnO<sub>2</sub> coating). The existence of these materials indicates that the pure oxidation of Mn<sup>2+</sup> occurs during the process of depositing MnO<sub>2</sub> onto the surface of PbO<sub>2</sub> and a variety of different substances are found between the interfaces.

### 3.3. XPS analysis

Fig. 4 presents the XPS results of the Ti/MnO<sub>2</sub> anodes electrodeposited in different plating solutions. Fig. 4a shows the Mn2p region of the S-MnO<sub>2</sub> spectrum. The two peaks at 653.7 eV and 642.0 eV correspond to the Mn2p<sub>3/2</sub> and Mn2p<sub>1/2</sub> orbitals, respectively. Fig. 4c shows the Mn2p region of the N-MnO<sub>2</sub> spectrum at 653.8 eV and 642.1 eV. The two peaks correspond to the Mn2p<sub>3/2</sub> and Mn2p<sub>1/2</sub> orbitals, respectively. The binding energy of S-MnO<sub>2</sub> and N-MnO<sub>2</sub> in the Mn2p region is 11.7 eV, which is the peak of typical MnO<sub>2</sub>,<sup>16</sup> indicating that +4 is the primary valence of manganese. In addition, a small amount of manganese element with +3 valence and +5 valence is present.<sup>17</sup> The O1s spectrum of S-MnO<sub>2</sub> is shown in Fig. 4b. The binding peaks at 529.66, 531.09 and 532.12 eV correspond to Mn–O–Mn, Mn–OH and H–O–H, respectively. The O 1s spectrum of N-MnO<sub>2</sub> is shown in Fig. 4d. The binding peaks at 529.76, 531.01 and 532.22 eV correspond to Mn–O–Mn, Mn–OH and H–O–H, respectively. The peak binding energy of Mn–O–Mn for N-MnO<sub>2</sub> is higher than that for S-MnO<sub>2</sub>. It has shorter Mn–Mn distances, exhibits increased tunnelling probability for N-MnO<sub>2</sub>, and consequently, increased conductivity.<sup>18</sup> Furthermore, the peak spectrum of the two MnO<sub>2</sub> in the O 1s region indicates that the manganese oxide layer also contains hydroxide and crystal water, which are beneficial for increasing ionic conductivity,

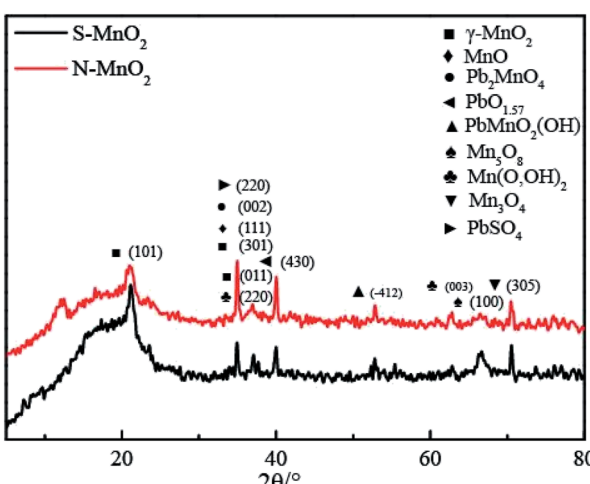


Fig. 3 XRD patterns of Ti/MnO<sub>2</sub> anodes electrodeposited at different plating solution.



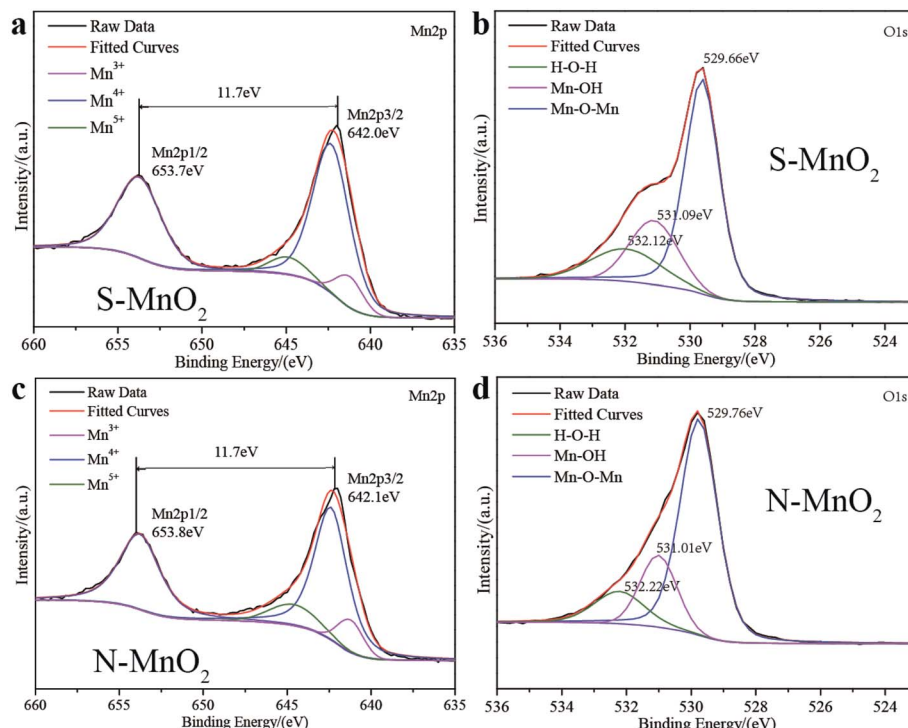


Fig. 4 XPS patterns of Ti/Sn-Sb-RuO<sub>x</sub>/β-PbO<sub>2</sub>/MnO<sub>2</sub> coatings electrodeposited at different plating solution (a and b) S-MnO<sub>2</sub> coating, (c and d) N-MnO<sub>2</sub> coating. Mn 2p spectrogram (a and c), O 1s spectrogram (b and d).

and thus, improve the activity and utilisation of manganese oxide. The incorporation of lead with semiconducting properties affects the bonding state of Mn-O and the water of crystallisation in the MnO<sub>2</sub> lattice, causing chemical shifts in the Mn 2p<sub>3/2</sub> level and increasing the binding energy. That is, Mn-O ionicity increases, covalency decreases and it is difficult to reduce; thus, the N-MnO<sub>2</sub> coating is more stable than the S-MnO<sub>2</sub> coating.<sup>19</sup>

The peak area obtained by Gaussian fitting of the peak indicates the relative content of each component. The relative percentages of different valence manganese elements are listed in Table 1.

From the data in Table 1, the trivalent manganese oxide content of N-MnO<sub>2</sub> is greater than the oxide content of S-MnO<sub>2</sub>. A complex oxide with a helical structure and that lacks cations in the crystal structure is formed. Therefore, the specific surface area of the MnO<sub>2</sub> crystal and the activity of the redox reaction are increased.<sup>18</sup>

### 3.4. Deposition mechanism of MnO<sub>2</sub>

Fig. 5a shows the CV curves of the Ti/Sn-Sb-RuO<sub>x</sub>/PbO<sub>2</sub> electrodes in the Mn(NO<sub>3</sub>)<sub>2</sub> and MnSO<sub>4</sub> baths at a scan rate of 5 mV

s<sup>-1</sup> at 60 °C. A potential range of 0–1.9 V (versus SCE) is used. The PbO<sub>2</sub> electrodes exhibit an evident symmetry on the CV curve in the MnSO<sub>4</sub> bath. An oxidation peak occurs between 1.00 V and 1.40 V. The PbO<sub>2</sub> electrodes present an evident asymmetry on the CV curve in the Mn(NO<sub>3</sub>)<sub>2</sub> plating solution, and a negative current value appears at 1.00–1.18 V. Then, the current rapidly rises to a positive value, and a large peak current occurs at 1.25 V. Finding that the current intensity of the oxidation peak between 1.20 V and 1.40 V in the Mn(NO<sub>3</sub>)<sub>2</sub> plating solution is higher than that in the MnSO<sub>4</sub> plating system is not difficult.

Owen *et al.*<sup>20</sup> confirmed the deposition mechanism in the sulphuric acid system as follows:

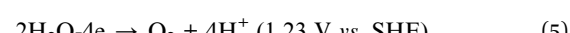
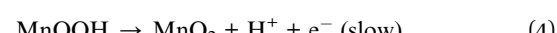
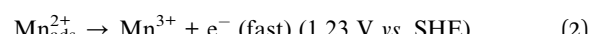


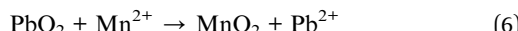
Table 1 XPS analytical results of manganese in S-MnO<sub>2</sub> and N-MnO<sub>2</sub>

Manganese element	Mn(III)	Mn(IV)	Mn(V)
S-MnO <sub>2</sub> -position/eV (relative content/%)	641.23 (10.7%)	642.32 (80.93%)	644.9 (8.37%)
N-MnO <sub>2</sub> -position/eV (relative content/%)	641.23 (11.12%)	642.39 (74.6%)	644.62 (14.28%)



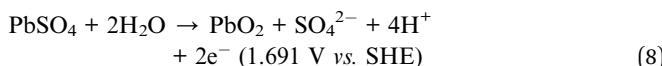
When the reaction in the deposition mechanism corresponds with the oxidation peak of the CV curve in the plating solution, the broadening oxidation peak within the range of 1.00–1.40 V on the curve includes reactions (2), (3) and (4). Given that OER (5) has the same standard equilibrium potential as reaction (2), the oxidation peak at 1.00–1.40 V is considered to correspond not only to the anodic electrodeposition reaction of  $\text{MnO}_2$  but also to the superposition of the OER peak. The anodic electrodeposition process of  $\text{MnO}_2$  competes with the OER within the potential range of 1.0–1.4 V.

The deposition of  $\text{MnO}_2$  onto the surface of the  $\text{PbO}_2$  electrode under acidic and high temperature conditions yields the following reaction:<sup>21</sup>



According to the reaction formula, during the deposition process,  $\text{PbO}_2$  is partially dissolved in the plating solution to form  $\text{Pb}^{2+}$ , and  $\text{Pb}^{2+}$  and  $\text{Mn}^{2+}$  are co-deposited under electrodepositing conditions to form  $(\text{Pb}, \text{Mn})$  oxide solid solution, which improves the stability of the electrode.<sup>22,23</sup>

However, the preceding reaction is difficult to perform in a sulphuric acid system.



From the reaction formulas (8) and (9),  $\text{PbO}_2$  is a spontaneous reaction in the  $\text{Mn}^{2+}$ -containing solution. The reaction

experiences difficulty in proceeding because the product  $\text{PbSO}_4$  is a poorly soluble substance that adheres to the surface of  $\text{PbO}_2$ . This condition hinders the continuation of the reaction. A possible scheme for the formation of porous  $\beta\text{-PbO}_2$  on the  $\text{Ti/Sn-Sb-RuO}_x$  electrode is illustrated in Fig. 5b and c. Under high voltage and high current density,  $\text{PbSO}_4$  is converted into one part of  $\text{PbO}_2$  and  $\text{MnO}_2$  is deposited on the other part. Therefore, in the interface between  $\text{MnO}_2$  and  $\text{PbO}_2$  deposited by the sulphuric acid system, an extremely thin layer of or nearly no  $\text{PbSO}_4$  is found. The obtained  $\text{MnO}_2$  film layer is thicker. However, the dissolution of  $\text{PbO}_2$ , *i.e.* surface  $\text{MnO}_2$  deposition, occurs during the volumetric electrodeposition of  $\text{MnO}_2$ . A mutual competition results in the presence of  $(\text{Pb}, \text{Mn})\text{O}_x$  in the interfacial layer of  $\text{MnO}_2$  and  $\text{PbO}_2$ , and the deposited  $\text{MnO}_2$  film is thin.

### 3.5. Electrochemical examination

The electrocatalytic properties of the obtained materials are highly correlated with OER. The rate of oxygen evolution can change in accordance with nature and surface microstructure. The change in anode materials properties in relation to OER primarily depends on changes in the roughness and chemical properties of oxide surface, which, in turn, lead to a change in bond strength of the oxygen-containing species chemisorbed onto the electrode surface.<sup>24</sup> The anodic polarisation curves of the  $\text{Ti/MnO}_2$  electrodes tested in  $50 \text{ g L}^{-1} \text{ Zn}^{2+}$  and  $150 \text{ g L}^{-1} \text{ H}_2\text{SO}_4$  solution are shown in Fig. 6 for the electrodes prepared using the electrodeposition method in the manganese sulphate and manganese nitrate plating solutions, respectively. The scan rate of the anodic polarisation curve in a synthetic electrolyte at  $40^\circ\text{C}$  is  $5 \text{ mV s}^{-1}$ , and the potential range is  $0$ – $1.9 \text{ V}$  (*versus* SCE), showing that both electrodes exhibit similar oxygen evolution

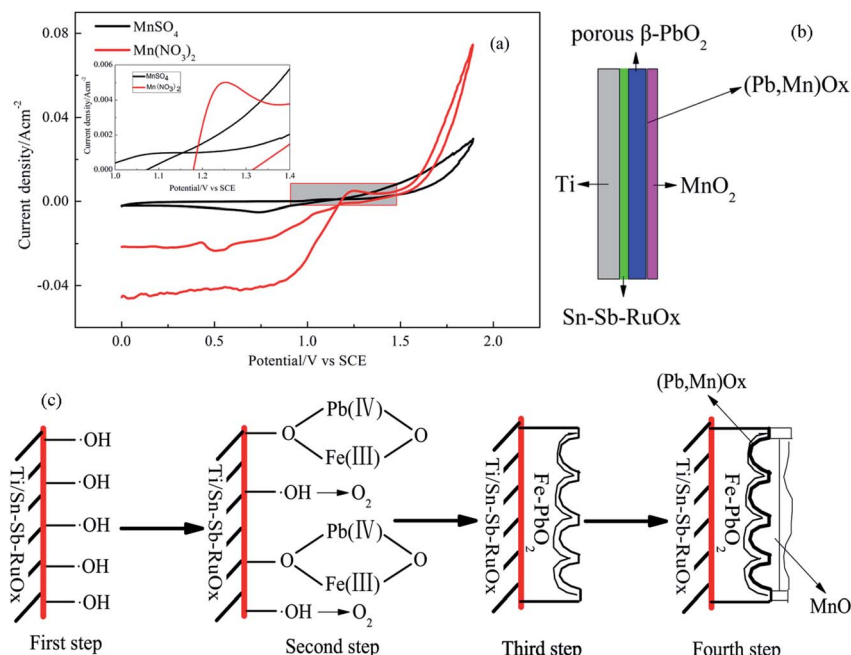


Fig. 5 The cyclic voltammetry curves and a possible scheme of deposition mechanism of  $\text{MnO}_2$ , (a) cyclic voltammetry curve, (b) schematic diagram of  $\text{Ti/Sn-Sb-RuO}_x/\beta\text{-PbO}_2/\text{MnO}_2$  electrode and (c) schematic mechanism of the electrodepositing N- $\text{MnO}_2$  coating.



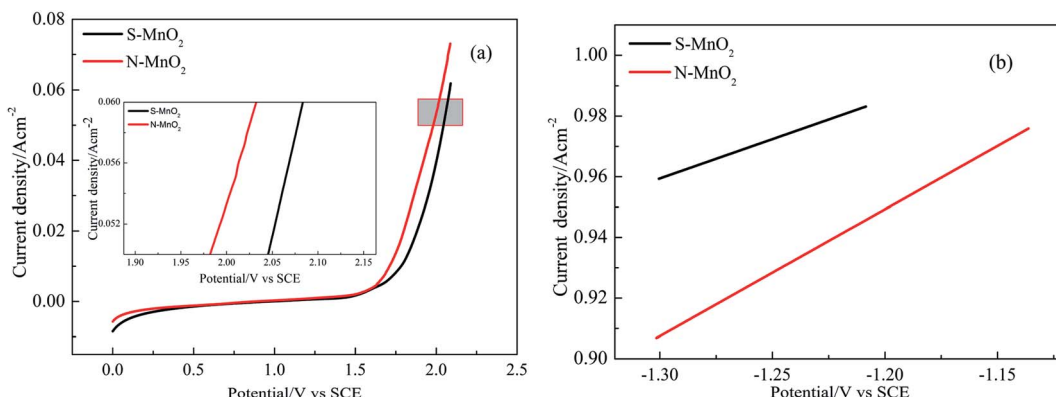


Fig. 6 Anodic polarization curves and Tafel lines for  $\text{Ti/Sn-Sb-RuO}_x/\beta\text{-PbO}_2/\text{MnO}_2$  electrodes, (a) anodic polarization curves, (b) the fitted Tafel lines.

behaviour. At a current density of  $0.05 \text{ A cm}^{-2}$ , the oxygen evolution potentials of  $\text{N-MnO}_2$  and  $\text{S-MnO}_2$  are  $1.982 \text{ V}$  and  $2.045 \text{ V}$ , respectively. After  $\text{MnO}_2$  is deposited onto the surface of the  $\text{Ti/Sn-Sb-RuO}_x/\beta\text{-PbO}_2$  intlayer, the oxygen evolution potential of  $\text{S-MnO}_2$  is  $63 \text{ mV}$  lower than that of  $\text{N-MnO}_2$ .

The Tafel fitting curve of the polarisation curve is also shown in Fig. 6b. The overpotential ( $\eta$ ) and logarithm for current density ( $\lg i$ ) used for the fitted Tafel lines are obtained using eqn (10):<sup>25-27</sup>

$$\eta = E + 0.2415 - 1.241 - JR_s \quad (10)$$

where  $E$  represents the oxygen evolution potential of the electrode (*versus* SCE).  $0.242 \text{ V}$  (*versus* SCE) is the potential of SCE.  $1.241 \text{ V}$  (*versus* the standard hydrogen electrode) is the reversible potential of oxygen evolution calculated from the Nernst equation used in a synthetic zinc electrolyte of  $50 \text{ g L}^{-1} \text{ Zn}^{2+}$  and  $150 \text{ g L}^{-1} \text{ H}_2\text{SO}_4$  at  $40 \text{ }^\circ\text{C}$ .  $J$  is the faradaic current, and  $R_s$  represents the solution resistance.

The overpotential  $\eta$  and the current density  $i$  have a logarithmic relationship of the eqn (11):

$$\eta = a + b \lg i \quad (11)$$

where  $\eta$  and  $i$  represent the overpotential of oxygen evolution and the faradaic current, respectively. Meanwhile,  $a$ ,  $b$  are Tafel parameters.

In addition, the relationship between the Tafel parameters  $a$ ,  $b$  and the exchange current  $i_0$  is as in eqn (12) and (13).

$$a = -2.3 \frac{RT}{\beta nF} \lg i_0 \quad (12)$$

$$b = 2.3 \frac{RT}{\beta nF} \quad (13)$$

where  $R$  is the general gas constant,  $T$  is the absolute temperature,  $\beta$  is the transfer coefficient,  $n$  is the electron number for the electrode reaction,  $F$  is the Faraday constant current and  $i_0$  is the exchange current density.

From the general formulas, *i.e.* eqn (10)–(13), the values of  $a$  and  $b$  and the exchange current density  $i_0$  are obtained by

fitting the anodic polarisation curve with the origin 8.5, and the results are provided in Table 2. The exchange current density is the most important parameter in studying the electrocatalytic activity of the electrode in the dynamics of the electrode process. In general, the electrocatalytic activity of the electrode is higher when the exchange current density is higher.<sup>26</sup> Therefore, from the data in Table 2, the exchange current density of  $\text{S-MnO}_2$  and  $\text{N-MnO}_2$  are  $1.003 \times 10^{-5} \text{ A cm}^{-2}$  and  $3.371 \times 10^{-4} \text{ A cm}^{-2}$ , respectively, and the  $\text{N-MnO}_2$  electrode achieves the highest catalytic activity. Some cracks in the  $\text{MnO}_2$

Table 2 Anodic polarization curve fitting value of  $\text{Ti/MnO}_2$  anodes electrodeposited at different plating solution

Samples	$\eta/\text{V}$ (at $500 \text{ A m}^{-2}$ )	$a/\text{V}$	$b/\text{V}$	$i_0 (\text{A cm}^{-2})$
$\text{S-MnO}_2$	0.969	1.297	0.259	$1.003 \times 10^{-5}$
$\text{N-MnO}_2$	0.896	1.451	0.418	$3.371 \times 10^{-4}$

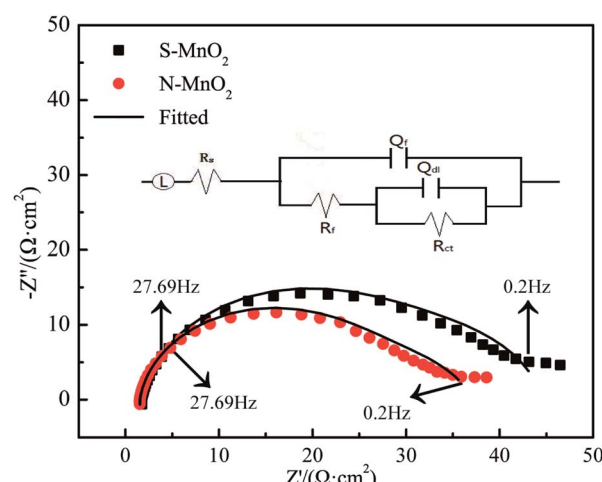


Fig. 7 EIS of  $\text{Ti/MnO}_2$  anodes electrodeposited at different plating solution.



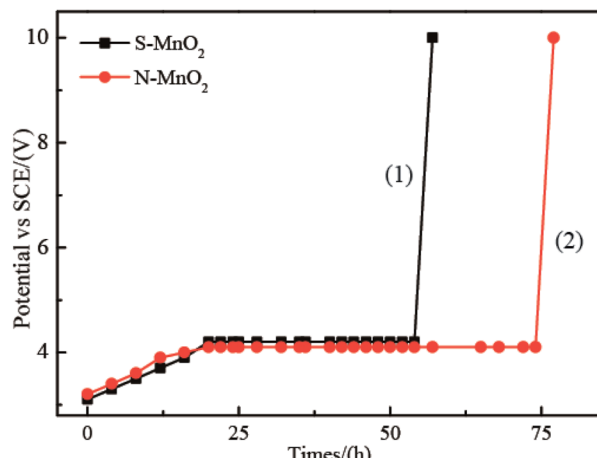


Fig. 8 Accelerated life study of Ti/MnO<sub>2</sub> anodes electrodeposited at different plating solution: (1) S-MnO<sub>2</sub>; (2) N-MnO<sub>2</sub>.

coating may result in contact between the solution (50 g L<sup>-1</sup> Zn<sup>2+</sup> + 150 g L<sup>-1</sup> H<sub>2</sub>SO<sub>4</sub>) and MnO<sub>2</sub> and/or (Pb, Mn)O<sub>x</sub>. However, given that the (Pb, Mn)O<sub>x</sub> and MnO<sub>2</sub> layers have highly similar oxygen evolution potential values,<sup>10</sup> the contribution of these oxides cannot be determined.

To evaluate the oxygen evolution activity of different MnO<sub>2</sub> electrodes, EIS measurements are performed at constant potential (1.5 V) in the OER potential domain. Fig. 7 and 8 respectively show the Nyquist, Bode and phase angle plots of the S-MnO<sub>2</sub> and N-MnO<sub>2</sub> electrodes in the 50 g L<sup>-1</sup> Zn<sup>2+</sup> + 150 g L<sup>-1</sup> H<sub>2</sub>SO<sub>4</sub> solution.

The electrochemical impedance spectra of the two electrodes are extremely similar. They are composed of two capacitive reactance arcs, which consist of the capacitive reactance arc in the high-frequency region and the semicircular arc in the low-frequency region. However, the capacitive reactance arc size of each electrode is different. In the low-frequency region, the capacitive reactance arc is relatively large, indicating that the electrode is caused by OER occurring at the interface between the oxide coating and the solution.<sup>28</sup> Meanwhile, the high-frequency impedance is related to the properties of the oxide film.<sup>29</sup> A typical order of this type of magnitude inductance is 1  $\mu$ H, which exhibits good agreement with that observed in the current work.<sup>30</sup>  $R_s$  indicates the resistance of the solution, and the parallel ( $R_{ct}Q_{dl}$ ) combination presents the behaviour of the interface between the oxide and the electrolyte. Meanwhile, the ( $R_fQ_f$ ) combination describes the properties of the oxide film. Other EIS parameters are listed in Table 3, where  $R_{ct}$  and  $R_f$  are the charge transfer resistance and film resistance, respectively, and  $Q$  denotes the constant phase elements (CPES). CPE is

generally believed to be derived from the distribution of current density along the surface of the electrode as a result of surface inhomogeneity. This phenomenon can be inferred from the analogy with the behaviour of the porous electrodes.<sup>31</sup> CPE is used to consider the phase shift impedance of the frequency between the applied AC potential and its current response.  $Y$  is defined using eqn (14):<sup>32</sup>

$$Y = Y_0(j\omega)^n \quad (14)$$

where  $Y_0$  and  $n$  are the CPE constant and exponent, respectively;  $\omega$  is the angular frequency in rad s<sup>-1</sup> ( $\omega = 2\pi f$ ) and  $j^2 = -1$  is an imaginary number. An  $n$  value of zero corresponds to a pure resistor. A unity value of  $n$  corresponds to a pure capacitor. An  $n$  value of 0.5 corresponds to Warburg impedance. The evident semicircles are related to the electrochemical oxidation of H<sub>2</sub>O into O<sub>2</sub>. The diameter of a semicircle is denoted by  $R_{ct}$ . The  $R_{ct}$  values of N-MnO<sub>2</sub> and S-MnO<sub>2</sub> are approximately 26.94  $\Omega$  cm<sup>2</sup> and 30.73  $\Omega$  cm<sup>2</sup>, respectively. The results show that the N-MnO<sub>2</sub> electrode exhibits high activity towards the electrochemical oxidation of H<sub>2</sub>O compared with the S-MnO<sub>2</sub> electrode. An explanation for the high electrochemical activity of oxygen evolution is that additional active surface sites are present in the N-MnO<sub>2</sub> electrode.<sup>33</sup> The results agree with that of a previous study,<sup>34</sup> which reported that an electrode with low  $R_{ct}$  exhibits high oxygen evolution activity.

$$Q_{dl} = (C_{dl})^n [(R_s)^{-1} + (R_{ct})^{-1}]^{(1-n)} \quad (15)$$

The  $C_{dl}$  values are obtained from the  $Q_{dl}$  values by using eqn (15), and  $n$  denotes the degree of deviation from the perfect capacitor.<sup>35</sup> Alves reported a new approach for the *in situ* characterisation of rough/porous oxide electrodes.<sup>36</sup> On the basis of the reported procedure, the double layer capacitance,  $C_{dl}$ , can be used as a relative measure of the electrode surface area.

Table 3 provides the  $C_{dl}$  and roughness factors ( $R_F$ ) of the anodes.  $R_F$  can be calculated using eqn (16):<sup>37</sup>

$$R_F = \frac{C_{dl}}{C^*} \quad (16)$$

where  $C^*$ , an assumed reference value for the capacitance, is proposed to be 20  $\mu$ F cm<sup>-2</sup> for smooth mercury electrodes.<sup>37</sup>

Table 4 Calculated capacitance and roughness factor

Electrodes	$C_{dl}/(\mu\text{F cm}^{-2})$	$R_F$
S-MnO <sub>2</sub>	770.5	38.525
N-MnO <sub>2</sub>	584.9	29.245

Table 3 EIS parameters of Ti/MnO<sub>2</sub> anodes electrodeposited at different plating solution

Anodes	$L$ ( $\mu$ H)	$R_s$ ( $\Omega$ cm <sup>2</sup> )	$R_{ct}$ ( $\Omega$ cm <sup>2</sup> )	$n_{dl}$	$Q_{dl}$ ( $\Omega^{-1}$ cm <sup>-2</sup> S <sup>n</sup> )	$R_F$ ( $\Omega$ cm <sup>2</sup> )	$n_f$	$Q_f$ ( $\Omega^{-1}$ cm <sup>-2</sup> S <sup>n</sup> )
S-MnO <sub>2</sub>	1.892	1.746	30.73	0.914	$1.367 \times 10^{-3}$	13.21	0.672	$2.463 \times 10^{-2}$
N-MnO <sub>2</sub>	1.907	1.538	26.94	0.919	$1.034 \times 10^{-3}$	8.596	0.749	$3.923 \times 10^{-2}$



The  $R_F$  values typically discovered in anodic oxide films are frequently due to their characteristic morphology.<sup>38</sup> In the present study, the  $R_F$  value obtained in the manganese nitrate system is lower than that in the manganese sulphate system (Table 4). This finding may be attributed to the presence of more cracks on the surface of the S-MnO<sub>2</sub> electrode, affecting surface roughness. Meanwhile,  $R_F$  is approximately 8.596  $\Omega \text{ cm}^2$  for the N-MnO<sub>2</sub> electrode. Its small  $R_F$  implies that the oxide coating exhibits excellent electrical conductivity, and the interlayer is largely affected.

### 3.6. Service life evaluation

Under ambient temperature and pressure, the service life of an electrode is affected by the concentration of corrosive substances, such as acids and halogen ions, current densities and the surface characteristics of the electrode.<sup>39</sup> As shown in Fig. 8, the trend of voltage change of the two electrodes is consistent during the accelerated life; that is, voltage rises in the beginning, remains stable and abruptly drops in the final stage, causing the electrode to fail.<sup>40</sup> Therefore, the failure mechanism of the Ti/MnO<sub>2</sub> electrode can be explained.<sup>41</sup> During long-time electrolysis, MnO<sub>2</sub> generates microcracks. Gas and solution wash these microcracks, causing the MnO<sub>2</sub> layer to peel off from the surface of PbO<sub>2</sub>, and the potential rises to the oxygen evolution potential of PbO<sub>2</sub>. At this moment, oxygen evolution occurs in the PbO<sub>2</sub> layer, and finally, the coating completely falls off.

To accelerate the study of service life, we apply a high concentration of Cl<sup>-</sup> (2 g L<sup>-1</sup>) and high current density (1 A cm<sup>-2</sup>). The results are presented in Fig. 8. From 0 h to 20 h, the cell voltage of the S-MnO<sub>2</sub> anode increases from 3.1 V to 4.2 V and then remains constant, indicating that the MnO<sub>2</sub> coating is partly broken and the interlayer is exposed. By contrast, with the gradual consumption of Cl<sup>-</sup> ions, the cell voltage of the N-MnO<sub>2</sub> anode remains stable until 74 h when both cell voltages increase linearly. Considering that the intermediate layer is basically consumed during the accelerated life test, the titanium matrix is oxidised to form a poorly conductive oxide, which increases ohmic losses. In the zinc EW industry, Cl<sup>-</sup> ions are ubiquitous in acidic zinc sulphate electrolyte solutions. Cl<sup>-</sup> ions in acidic zinc sulphate electrolyte solutions increase the corrosion rate and reduce the service life of anode plates.<sup>42</sup>

Table 5 Service accelerated life test results

Electrodes	Solution composition	Current densities (A cm <sup>-2</sup> )	Service life (h)	Ref.
N-MnO <sub>2</sub>	H <sub>2</sub> SO <sub>4</sub> (150 g L <sup>-1</sup> ) + Cl <sup>-</sup> (2 g L <sup>-1</sup> )	1.0	77	This work
S-MnO <sub>2</sub>	H <sub>2</sub> SO <sub>4</sub> (150 g L <sup>-1</sup> ) + Cl <sup>-</sup> (2 g L <sup>-1</sup> )	1.0	57	This work
Ti/Sn-Sb-Ru/β-PbO <sub>2</sub>	H <sub>2</sub> SO <sub>4</sub> (150 g L <sup>-1</sup> ) + Cl <sup>-</sup> (2 g L <sup>-1</sup> )	1.0	68	48
Ti-Sn/Sb/RuO <sub>2</sub> -β-PbO <sub>2</sub>	H <sub>2</sub> SO <sub>4</sub> (0.5 M)	4.0	48	49
Ti/Sb-SnO <sub>2</sub> /β-PbO <sub>2</sub>	H <sub>2</sub> SO <sub>4</sub> (1 M)	1.0	23	50
Ti/Sb-SnO <sub>2</sub> /β-PbO <sub>2</sub> -Ce	H <sub>2</sub> SO <sub>4</sub> (1 M)	1.0	45	50
Ti/Sb-SnO <sub>2</sub> /β-PbO <sub>2</sub> -Nd	H <sub>2</sub> SO <sub>4</sub> (1 M)	1.0	48	50
Ti/Sb-SnO <sub>2</sub> /β-PbO <sub>2</sub> -Gd	H <sub>2</sub> SO <sub>4</sub> (1 M)	1.0	28	50
Ti/Sb-SnO <sub>2</sub> /β-PbO <sub>2</sub> -Sm	H <sub>2</sub> SO <sub>4</sub> (1 M)	1.0	37	50
Ti/SnO <sub>2</sub> -Sb <sub>2</sub> O <sub>3</sub> /PbO <sub>2</sub>	H <sub>2</sub> SO <sub>4</sub> (1 M)	1.0	65	51
Ti/SnO <sub>2</sub> -Sb <sub>2</sub> O <sub>3</sub> /MnO <sub>2</sub>	H <sub>2</sub> SO <sub>4</sub> (1 M)	1.0	31	51

Therefore, investigating the influence of Cl<sup>-</sup> ions on the service life of the β-PbO<sub>2</sub> electrode is meaningful from a practical perspective.

The N-MnO<sub>2</sub> anode has a longer service life under high current density than the S-MnO<sub>2</sub> anode. This result is further compared with the lead dioxide anodes prepared by other researchers, as shown in Table 5, where the concentration of all Cl<sup>-</sup> ions is 1 g L<sup>-1</sup> Cl<sup>-</sup>. We conclude that the N-MnO<sub>2</sub> anode is sufficiently stable to be used as an electrode. Many factors can affect electrode stability. Firstly, the dense and thin layer of N-MnO<sub>2</sub> that can form on the surface of the PbO<sub>2</sub> anode can achieve good adherence; it is also nonconductive, and thus, protects the underlying anode.<sup>43</sup> An anode that is coated with MnO<sub>2</sub> has a significantly lower operating voltage than typical anodes.<sup>44</sup> However, if excessive MnO<sub>2</sub> (for S-MnO<sub>2</sub>) forms on the anode surface, then it may not sufficiently adhere and may spall from the surface. Secondly, the crack of the N-MnO<sub>2</sub> coating is relatively narrow, and the crack of the S-MnO<sub>2</sub> coating is sharp and wide. Although S-MnO<sub>2</sub> presents good spherical cell morphology and constitutes a large specific surface area, the stacking of such simple spherical particles is evidently unstable, and the contact area between these particles is small, resulting in a weak bond between the plating layer and PbO<sub>2</sub>, causing the latter to fall off easily.<sup>45</sup> Thirdly, compared with the lead alloy anode, the MnO<sub>2</sub> deposited on the lead alloy anode decreases the evolution rate of chlorine, and the MnO<sub>2</sub> anode covering PbO<sub>2</sub> has low current efficiency and high oxygen evolution efficiency, probably due to MnO<sub>2</sub> forming a diffusional barrier to Cl<sup>-</sup> ions.<sup>46</sup> A study on oxygen and chlorine evolution from manganese oxide-coated dimensionally stable anodes<sup>47</sup> showed that anodic polarisation produced 'MnO<sub>2</sub>' results in nearly complete suppression of chlorine evolution as a result of the following: (a) an extremely low exchange current for chlorine evolution on the amorphous oxide layer and (b) the diffusion barrier provided by the oxide layer prevents access of Cl<sup>-</sup> ions to the underlying electrode surface.

## 4. Conclusion

MnO<sub>2</sub> coatings were successfully prepared on porous Ti/Sn-Sb-RuO<sub>x</sub>/β-PbO<sub>2</sub> substrates by electrodeposition in sulfate system and nitrate system using a low current density. The important



conclusion is that the composition of the electrodeposition solution may cause a significant change in the deposition mechanism during the  $\text{MnO}_2$  electrodeposition process, thereby changing the thickness of the deposited layer. SEM results show that Ti/ $\text{MnO}_2$  has a rough morphology and particle accumulation is very obvious. The morphology of N- $\text{MnO}_2$  under microscopic appearance is microscopically shaped, layered, and densely bonded. The grain size is 50–150 nm. S- $\text{MnO}_2$  is a ribbon-like. The surface of N- $\text{MnO}_2$  is more uniform than S- $\text{MnO}_2$ . The main crystal phase of  $\text{MnO}_2$  is  $\gamma$  type, and the main valence of  $\text{MnO}_2$  is +4 valence. In addition, a small amount of Mn element with +3 valence and +5 valence is present by XPS analysis.

The oxygen evolution potential of N- $\text{MnO}_2$  at 0.05 A  $\text{cm}^{-2}$  is 63 mV lower than that of S- $\text{MnO}_2$ , indicating that N- $\text{MnO}_2$  has better oxygen evolution electrocatalytic activity, which can also be confirmed by EIS test results. The embedded structure between porous Ti/Sn-Sb-RuO<sub>x</sub>/ $\beta$ -PbO<sub>2</sub> substrate and  $\text{MnO}_2$  coating can increase the stability of Ti/ $\text{MnO}_2$  electrode. The stability of N- $\text{MnO}_2$  is 77 h in a solution with 2 g  $\text{L}^{-1}$   $\text{Cl}^-$  and 150 g  $\text{L}^{-1}$   $\text{H}_2\text{SO}_4$  at 25 °C under 1 A  $\text{cm}^{-2}$ , which is more stable than the S- $\text{MnO}_2$ .

## Conflicts of interest

There are no conflicts to declare.

## Acknowledgements

This research is supported by Yunnan Fundamental Research Projects (grant No. 140520210048), the Natural Science Foundation of China (Project No. 51564029 and No. 51504111 and No. 51874154), the Technology Innovation Talents Project of Yunnan Province (No. 2019HB111), the construction of high-level talents of Kunming University of Science and Technology (KKKP201763019), and Research on Microwave Method in Carbon Fiber Preparation (KKK0201863053).

## References

- 1 M. Minakshi, D. Mitchell, M. L. Carter, *et al.*, Microstructural and spectroscopic investigations into the effect of CeO<sub>2</sub> additions on the performance of a  $\text{MnO}_2$  aqueous rechargeable battery, *Electrochim. Acta*, 2009, **54**, 3244–3249.
- 2 M. Minakshi, D. Mitchell and K. Prince, Incorporation of TiB<sub>2</sub> additive into  $\text{MnO}_2$  cathode and its influence on rechargeability in an aqueous battery system, *Solid State Ionics*, 2008, **179**, 355–361.
- 3 Y. Q. Wang, B. Gu, W. L. Xu and L. D. Lu, Effects of Preparation Conditions of MnO<sub>x</sub> Coatings on Characteristics of Ti/SnO<sub>2</sub> + Sb<sub>2</sub>O<sub>3</sub>/MnO<sub>x</sub> Anodes, *J. Inorg. Mater.*, 2006, **21**, 1362–1366.
- 4 A. Yusuf, C. Snape, J. He, H. Xu and S. Behera, Advances on transition metal oxides catalysts for formaldehyde oxidation: A review, *Catal. Rev.: Sci. Eng.*, 2017, **59**(3), 189–233.
- 5 M. M. Thackeray, Manganese oxides for lithium batteries, *Prog. Solid State Chem.*, 1997, **25**(1–2), 1–71.
- 6 Y. H. Shi, H. M. Meng and D. B. Sun, Progress of Ti based base metal oxide coating anode, *J. Funct. Mater.*, 2007, **38**, 2696–2699.
- 7 L. Mao, D. Zhang, T. Sotomura, K. N. Mechanisti, N. Koshiba and T. Ohsaka, study of the reduction of oxygen in air electrode with manganese oxides as electrocatalysts, *Electrochim. Acta*, 2003, **48**, 1015–1021.
- 8 Y. Q. Lai, Y. Li, L. X. Jiang, X. J. Lv, J. Li and Y. X. Liu, Electrochemical performance of a Pb/Pb-MnO<sub>2</sub> composite anode in sulfuric acid solution containing Mn<sup>2+</sup>, *Hydrometallurgy*, 2012, **115–116**, 64–70.
- 9 E. Preisler, Material problems encountered in anodic  $\text{MnO}_2$  deposition, *J. Appl. Electrochem.*, 1989, **19**, 559–565.
- 10 H. T. Yang, B. M. Chen and H. R. Liu, Effects of manganese nitrate concentration on the performance of analuminum substrate  $\beta$ -PbO<sub>2</sub>-MnO<sub>2</sub>-WC-ZrO<sub>2</sub> composite electrode material, *Int. J. Hydrogen Energy*, 2014, **39**, 3087–3099.
- 11 M. Panizza, I. Sirés and G. Cerisola, Anodic oxidation of mecoprop herbicide at lead dioxide, *J. Appl. Electrochem.*, 2008, **38**, 923–929.
- 12 L. Chang, Y. Zhou, X. Duan, W. Liu and D. Xu, Preparation and characterization of carbon nanotube and Bi co-doped PbO<sub>2</sub> electrode, *J. Taiwan Inst. Chem. Eng.*, 2014, **45**, 1338–1346.
- 13 B. M. Chen, S. C. Wang, J. H. Liu, H. Huang, C. Dong, Y. He, W. Yan, Z. Guo, R. Xu and H. Yang, Corrosion resistance mechanism of a novel porous Ti/Sn-Sb-RuO<sub>x</sub>/ $\beta$ -PbO<sub>2</sub> anode for zinc electrowinning, *Corros. Sci.*, 2018, **144**, 136–144.
- 14 E. Preisler, Electrodeposited manganese dioxide with preferred crystal growth, *J. Appl. Electrochem.*, 1976, **6**, 301–310.
- 15 L. Li, Z. Huang, X. Fan, Z. Zhang, R. Dou, S. Wen, Y. Chen, Y. Chen and Y. Hu, Preparation and Characterization of a Pd modified Ti/SnO<sub>2</sub>-Sb anode and its electrochemical degradation of Ni-EDTA, *Electrochim. Acta*, 2017, **231**, 354–362.
- 16 X. Y. Lang, A. Hirata, T. Fujita and M. W. Chen, Nanoporous metal/oxide hybrid electrodes for electrochemical supercapacitors, *Nat. Nanotechnol.*, 2011, **6**, 232–236.
- 17 M. M. Sundaram, A. Biswal, D. Mitchell, R. Jones and C. Fernandez, Correlation among physical and electrochemical behaviour of nanostructured electrolytic manganese dioxide from leach liquor and synthetic for aqueous asymmetric capacitor, *Phys. Chem. Chem. Phys.*, 2016, **18**, 4711–4720.
- 18 E. Preisler, Semiconductor properties of manganese dioxide, *J. Appl. Electrochem.*, 1976, **6**, 311–320.
- 19 H. J. Yao, X. M. Liu and X. G. Zhang, Nanophase PbTiO<sub>3</sub> modified MnO<sub>2</sub> electrode, *Chin. J. Appl. Chem.*, 2003, **20**, 336–340.
- 20 M. P. Owen, G. A. Lawrence and S. W. Donne, An electrochemical quartz crystal microbalance study into the deposition of manganese dioxide, *Electrochim. Acta*, 2007, **52**, 4630–4639.
- 21 Y. M. Yang and D. J. Yan, Exploration for the trends of the reaction of PbO<sub>2</sub> and Mn<sup>2+</sup>, *Nat. Sci.*, 2008, **29**, 403–408.



22 X. H. Zheng, M. M. Dai and G. R. Chen, The Anodic Behaviour of  $\text{MnO}_2$  and  $\text{PbO}_2$  Electrode Prepared by Simultaneous Electrodeposition, *Nat. Sci.*, 1998, **14**, 62–65.

23 J. Wang, R. D. Xu and B. H. Yu, Investigation on Electrochemical Behavior of  $\text{PbO}_2$  and  $\text{MnO}_2$  Co-deposition, *Mater. Rep.*, 2017, **31**, 35–40.

24 O. Shmychkova, T. Luk'yanenko, A. Velichenko, L. Meda and R. Amadelli, Bi-doped  $\text{PbO}_2$  anodes: Electrodeposition and physico-chemical properties, *Electrochim. Acta*, 2013, **111**, 332–338.

25 H. Yang, B. Chen, Z. Guo, H. Liu, Y. Zhang, H. Huang, R. Xu and R. Fu, Effects of current density on preparation and performance of Al/conductive coating/ $\alpha$ - $\text{PbO}_2$ - $\text{CeO}_2$ - $\text{TiO}_2$ / $\beta$ - $\text{PbO}_2$ - $\text{MnO}_2$ - $\text{WC}$ - $\text{ZrO}_2$  composite electrode materials, *Trans. Nonferrous Met. Soc. China*, 2014, **24**, 3394–3404.

26 Y. Lai, Y. Li, L. Jiang, W. Xu, X. Lv, J. Li and Y. Liu, Electrochemical behaviors of co-deposited  $\text{Pb}/\text{Pb}-\text{MnO}_2$  composite anode in sulfuric acid solution-Tafel and EIS investigations, *J. Electroanal. Chem.*, 2012, **671**, 16–23.

27 H. Ning, Y. Xin and L. Xu, Properties of  $\text{IrO}_2$ - $\text{Ta}_2\text{O}_5$  Coated Titanium Anodes Modified with Graphene, *Rare Met. Mater. Eng.*, 2016, **45**, 946–951.

28 Z. G. Ye, H. Y. Liu, X. L. Zhou, X. Z. Hua and X. Y. Peng, Effect of cooling mode on electrocatalytic activity and stability of  $\text{Ti}/\text{IrO}_2 + \text{MnO}_2$  anodes, *J. Funct. Mater.*, 2011, **42**, 264–268.

29 L. K. Xu and J. D. Scantlebury, A study on the deactivation of an  $\text{IrO}_2$ - $\text{Ta}_2\text{O}_5$  coated titanium anode, *Corros. Sci.*, 2003, **45**, 2729–2740.

30 A. Biswal, P. K. Panda, A. N. Acharya, *et al.*, Role of Additives in Electrochemical Deposition of Ternary Metal Oxide Microspheres for Supercapacitor Applications, *ACS Omega*, 2020, **5**(7), 3405–3417.

31 G. J. Brug, A. L. G. van den Eeden, M. Sluyters-Rehbach and J. H. Sluyters, The analysis of electrode impedances complicated by the presence of a constant phase element, *J. Electrochem. Soc.*, 1984, **176**, 275–295.

32 Y. B. Hu, C. F. Dong, M. Sun, K. Xiao, P. Zhong and X. G. Li, Effects of solution pH and  $\text{Cl}^-$  on electrochemical behaviour of an Aermet100 ultra-high strength steel in acidic environments, *Corros. Sci.*, 2011, **53**, 4159–4165.

33 H. T. Yang, B. M. Chen, Z. C. Guo, H. Huang, R. D. Xu and R. C. Fu, Effects of current density on preparation and performance of Al/conductive coating/ $\alpha$ - $\text{PbO}_2$ - $\text{CeO}_2$ - $\text{TiO}_2$ / $\beta$ - $\text{PbO}_2$ - $\text{MnO}_2$ - $\text{WC}$ - $\text{ZrO}_2$  composite electrode materials, *Trans. Nonferrous Met. Soc. China*, 2014, **24**, 3394–3404.

34 Z. Yan, Y. Zhao, Z. Zhang, G. Li, H. Li, J. S. Wang, Z. Q. Feng, M. Q. Tang, X. J. Yuan, R. Z. Zhang and Y. Y. Du, A study on the performance of  $\text{IrO}_2$ - $\text{Ta}_2\text{O}_5$  coated anodes with surface treated Ti substrates, *Electrochim. Acta*, 2015, **157**, 345–350.

35 V. Alves, L. Silva and J. Boodts, Surface characterisation of  $\text{IrO}_2/\text{TiO}_2/\text{CeO}_2$  oxide electrodes and Faradaic impedance investigation of the oxygen evolution reaction from alkaline solution, *Electrochim. Acta*, 1998, **44**, 1525–1534.

36 V. A. Alves, L. A. D. Silva and J. F. C. Boodts, Surface characterisation of  $\text{IrO}_2/\text{TiO}_2/\text{CeO}_2$  oxide electrodes and faradaic impedance investigation of the oxygen evolution reaction from alkaline solution, *Electrochim. Acta*, 1998, **44**, 1525–1534.

37 R. De Levie, On porous electrodes in electrolyte solutions: I. Capacitance effects, *Electrochim. Acta*, 1963, **8**, 751–780.

38 U. Casellato, S. Cattarin and M. Musiani, Preparation of porous  $\text{PbO}_2$  electrodes by electrochemical deposition of composites, *Electrochim. Acta*, 2000, **48**, 3991–3998.

39 X. Chen and G. Chen, Stable  $\text{Ti}/\text{RuO}_2$ - $\text{Sb}_2\text{O}_5$ - $\text{SnO}_2$  electrodes for  $\text{O}_2$  evolution, *Electrochim. Acta*, 2005, **50**, 4155–4159.

40 H. S. Kong, *Research of some fundamental problems on stability of titanium substrate lead dioxide electrodes ( $\text{Ti}/\text{PbO}_2$ )*, Doctoral Dissertation of Jilin University, 2013, pp. 32–33.

41 Z. F. Chen and H. Y. Jiang, The effect of electrodeposition conditions of manganese dioxide and heat treatment of  $\text{PbO}_2$ - $\text{Ti}/\text{MnO}_2$  electrode on its catalytic and lifetime, *J. Cent.-South Inst. Min. Metall.*, 1991, **22**, 207–214.

42 H. T. Yang, Z. C. Guo, B. M. Chen, H. R. Liu, Y. C. Zhang, H. Huang, X. L. Li, R. C. Fu and R. D. Xu, Electrochemical behavior of rolled  $\text{Pb}-0.8\%\text{Ag}$  anodes in an acidic zinc sulfate electrolyte solution containing  $\text{Cl}^-$  ions, *Hydrometallurgy*, 2014, **147**–**148**, 148–156.

43 M. Tunnicliffe, F. Mohammadi and A. Alfantazi, Polarization behaviour of leadsilver anodes in zinc electrowinning electrolytes, *J. Electrochem. Soc.*, 2012, **159**, C170–C180.

44 G. Eggett and D. Naden, Developments in anodes for pure copper electrowinning from solvent extraction produced electrolytes, *Hydrometallurgy*, 1975, **1**, 123–137.

45 K. N. Cheng, *Metal anodes*, Shanghai, East China Normal University Press, 1989.

46 G. H. Kelsall, E. Guerra, G. Li and M. Bestetti, Effects of manganese (II) and chloride ions in zinc electrowinning reactors, *Electrochim. Soc. Proc.*, 2000, **14**, 350–361.

47 J. E. Bennett, Electrodes for generation of hydrogen and oxygen from seawater, *Int. J. Hydrogen Energy*, 1980, **5**, 401–408.

48 S. C. Wang, S. Chen and B. M. Chen, Effect of current densities on the microstructure and electrochemical behavior of the porous  $\beta$ - $\text{PbO}_2$  electrode, *Mater. Sci. Forum*, 2019, **956**, 21–34.

49 Y. Zheng, W. Su, S. Chen, X. Wu and X. Chen,  $\text{Ti}/\text{SnO}_2$ - $\text{Sb}_2\text{O}_5$ - $\text{RuO}_2$ / $\alpha$ - $\text{PbO}_2$ / $\beta$ - $\text{PbO}_2$  electrodes for pollutants degradation, *Chem. Eng. J.*, 2011, **174**, 304–309.

50 W. Yang, H. Wang and F. Fu, Preparation and performance of  $\text{Ti}/\text{Sb}-\text{SnO}_2$ / $\beta$ - $\text{PbO}_2$  electrode modified with rare earth, *Rare Met. Mater. Eng.*, 2010, **39**, 1215–1218.

51 L. Zhou and S. H. Shi, Preparation of Ti-based metal oxide electrode and its characteristics, *Environ. Prot. Chem. Ind.*, 2014, **34**, 84–89.

